Chemical Geology 606 (2022) 120974

Contents lists available at ScienceDirect

Chemical Geology

journal homepage: www.elsevier.com/locate/chemgeo

Mercury isotopes as a useful tracer of magma sources: An example from the Daocheng-Cuojiaoma batholith, eastern Tibetan Plateau

Zhendong Tian [a], Chengbiao Leng [b], Changzhou Deng [a], Xingchun Zhang [a], Di Chen [a,c], Lingjian Gao [a,d], Xueyun Wang [a,c], Runsheng Yin [a,*]

[a] State Key Laboratory of Ore Deposit Geochemistry, Institute of Geochemistry, Chinese Academy of Sciences, Guiyang 550081, China
[b] State Key Laboratory of Nuclear Resources and Environment, East China University of Technology, Nanchang 330013, China
[c] University of Chinese Academy of Sciences, Beijing 100049, China
[d] College of Earth Sciences, Jilin University, Changchun 130061, China

ARTICLE INFO

Editor: Don Porcelli

Keywords:
Mercury isotopes
Petrogenetic tracing
Magma mixing
Crust-mantle interactions

ABSTRACT

Magma mixing between mafic and felsic melts is a common magmatic process. Tracing the sources of different magma endmembers is often challenging using traditional isotopes, given the source isotopic signatures are often altered due to isotope fractionation. Mass-independent fractionation of mercury (Hg), which is predominantly generated during Hg photochemical reactions on Earth's surface with little influence from other processes, has the potential to be used as a petrogenetic tracer. This study investigates the Hg isotopic composition of mafic microgranular enclaves (MMEs) and their host granitoids from the Daocheng-Cuojiaoma batholith (DCGB), eastern Tibetan Plateau. Zircon U-Pb dating indicates both the host granitoids and two types of MMEs formed coevally at ca. 216–217 Ma, coherent to the subduction of Garzê–Litang paleo-Tethyan ocean. The host granitoids exhibit negative to slightly positive Δ^{199}Hg values (−0.20 to 0.02‰), indicating that their source magma was a mixture of terrestrial sediments- and mantle-derived melts. Type-I MMEs display arc-like trace element patterns, low SiO_2 (53.8 to 55.0 wt%) and positive Δ^{199}Hg values (0.00 to 0.10 ‰), indicating their derivation from a subduction-related fluid/melt metasomatized mantle source. Type-II MMEs show intervening concentrations of major/trace elements, and intermediate Δ^{199}Hg values (−0.18 to 0.02‰), suggesting they were generated via mixing of magmas for Type-I MMEs and granitoid. This study demonstrates the powerful use of Hg isotope as a tracer of magma sources during crustal-mantle interactions.

1. Introduction

Magma mixing plays a crucial role in generating the diversity of igneous rocks (Ruprecht et al., 2012). Recognizing the sources of different magma during mixing is often challenging using traditional Sr-Nd isotopes, given the initial isotopic signatures of different magmas are often altered due to chemical exchange and isotope fractionation (Lesher, 1990). A typical example of this can be the Daocheng-Cuojiaoma granitoid batholith (DCGB), which exposes over 5200 km^2, is one of the largest batholiths in the eastern Tibetan Plateau (He et al., 2013). Mafic microgranular enclaves (MMEs) are commonly observed in the DCGB. These MMEs evidence mixing of different magmas during the formation of the DCGB, however, due to these MMEs having Sr-Nd and zircon Hf isotope signals identical to the host granitoid (Wu et al., 2020; Dong et al., 2021), their magma sources remain poorly understood.

Mercury (Hg) isotopes have the potential for understanding the sources of magmas, as they undergo unique mass-independent fractionation (MIF, normally defined as Δ^{199}Hg), beside the common mass-dependent fractionation (MDF, δ^{202}Hg) (Blum et al., 2014). Hg-MIF occurs mainly during photochemical reactions with little interference from other processes (e.g., magmatic and hydrothermal processes) (Moynier et al., 2020, 2021; Wang et al., 2021b; Yin et al., 2022). The primitive mantle has shown near-zero Δ^{199}Hg (0.00 ± 0.10‰, Moynier et al., 2021). On Earth's surface, however, photochemical processes result in negative Δ^{199}Hg values in terrestrial reservoirs (−0.6 to 0 ‰, e.g., soil and vegetation) and positive Δ^{199}Hg values in oceanic reservoirs (−0.1 to 0.4 ‰, e.g., seawater and marine sediments) (Blum et al., 2014). Magmatic and hydrothermal processes do not trigger Hg-MIF, allowing the potential use of Hg-MIF signals for petrogenetic tracing. Recent studies observed non-zero Δ^{199}Hg values in mantle-derived

* Corresponding author.
E-mail address: yinrunsheng@mail.gyig.ac.cn (R. Yin).

https://doi.org/10.1016/j.chemgeo.2022.120974
Received 11 February 2022; Received in revised form 2 April 2022; Accepted 6 June 2022
Available online 9 June 2022

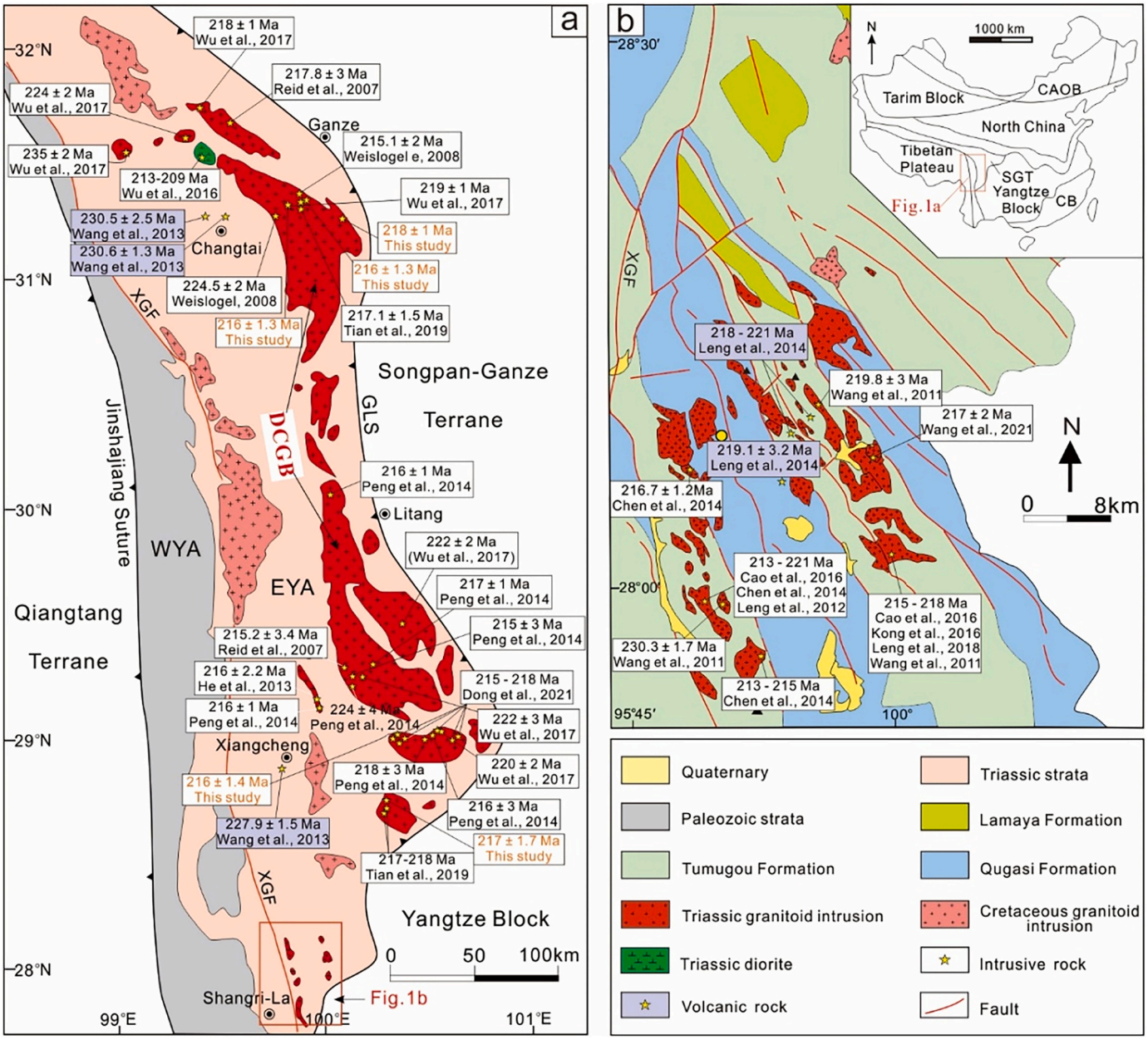

Fig. 1. (a) Simplified geological map of the Yidun arc showing the distribution of DCGB (after Tian et al., 2019). (b) Geological map of southern Yidun arc (after Leng et al., 2012). CAOB-Central Aisan Orogen Belt; CB-Cathaysian Block; EYA-Eastern Yidun Arc; GLS-Garzê-Litang Sutute; SGT-Songpan-Garzê Terrane; WAY-Western Yidun Arc; XGF-Xiangcheng-Geza Fault. Age data of granitic intrusion and volcanic rocks are from Cao et al. (2016), Chen et al. (2014), Kong et al. (2016), Leng et al. (2012, 2014, 2018), Peng et al. (2014), Reid et al. (2007), Tian et al. (2019), Wang et al. (2011, 2013b, 2021a), Weislogel (2008), and Wu et al. (2016, 2017).

igneous rocks (−0.45 to 0.37‰), highlighting the recycling of Hg from Earth's surface systems into the mantle (Moynier et al., 2021; Wang et al., 2021b; Yin et al., 2022).

To date, Hg isotopic studies regarding magma mixing remain lacking. The MMEs-containing granitoid in the DCGB provides a natural laboratory to test the applicability of using Hg isotope for magma source identification during magma mixing. This study investigated the isotope compositions of Hg in MMEs and granitoids in the DCGB. Combined with whole-rock major-trace elements, zircon U-Pb age, and mineral chemical composition analysis, we demonstrate that the DCGB was formed by mixing of (1) the upwelling enriched lithosphere mantle metasomatized by subduction-related fluid/melt and (2) the felsic melts produced by ancient terrestrial sediments.

2. Geological background

The Yidun arc in the eastern Tibetan Plateau (Fig. 1a) is bounded by the Jinshajiang Suture to the west and the Garzê–Litang Suture to the east. It is divided into the western Yidun arc (WYA, also called Zhongza microcontinent) and the eastern Yidun arc (EYA) by the NNW-trending Xiangcheng-Geza Fault (Fig. 1b). The WYA is composed of Paleozoic clastic and carbonate rocks, associated with late Permain mafic volcanic rock interlayers (Leng et al., 2014). These rocks underwent greenschist- to lower amphibolite-facies metamorphism in the early Triassic, due to the closure of the Jinshajiang Paleo-Tethyan Ocean and the resultant collision between the Qiangtang Terrane and WYA (Reid et al., 2007). Paleozoic sequences in the WYA have similar fossil assemblages to the coeval sedimentary successions in the western Yangtze Block, therefore, it is believed that the WYA was rifted from the western Yangtze Block

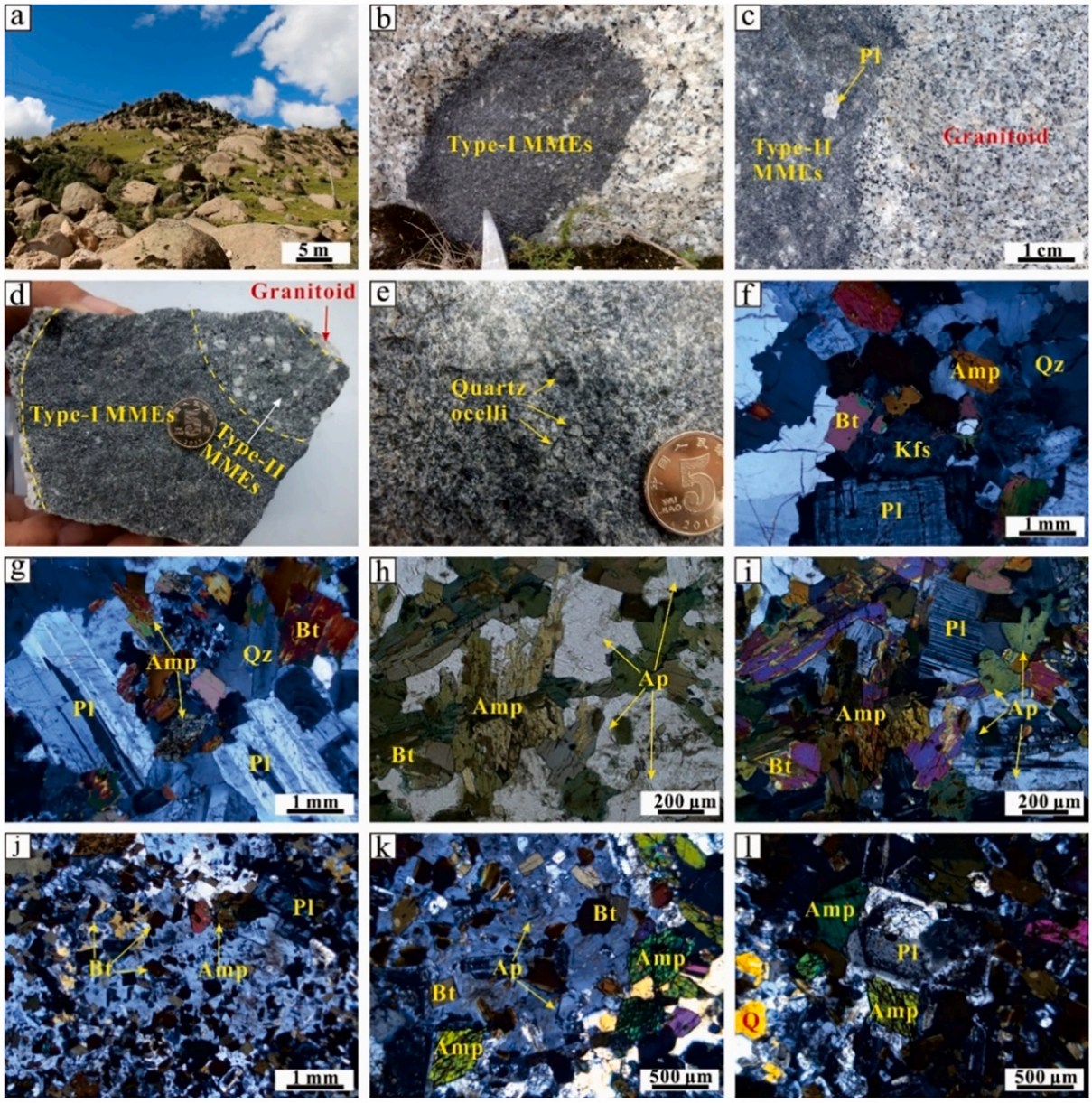

Fig. 2. (a) Field outcrop of granitoid from the DCGB; (b) Oval-shaped type-I MMEs within granitoid, showing sharp contact between them; (c) Plagioclase xenocryst in type-II MMEs; (d) Type-I MMEs transitional contact with the granitoid, with the transitional zone having similar petrographic and geochemical features to the type-II MMEs; (e) Quartz phenocryst rimed by fine-grained biotite and amphibole, forming quartz ocelli texture in the type-II MMEs; (f) Representative micro-photo of granitoid that is composed mainly of quartz, plagioclase, k-feldspar, amphibole, and biotite; (g) Plagioclase develops oscillatory zoning in the host granitoid; (h-i) Type-I MMEs consisting mainly of plagioclase, amphibole, and biotite, with abundant acicular apatite within the plagioclase and amphibole crystals; (j) Typical micro-photo of type-II MMEs showing fine-grained hypidiomorphic texture; (k) Acicular apatite within plagioclase phenocrysts from the type-II MMEs; (l) Plagioclase crystal from type-II MMEs showing absorbed texture. Mineral abbreviations: Amp-amphibole; Ap-apatite; Bt-biotite; Kfs-K-feldspar; Pl-plagioclase; Qz-quartz.

owing to the opening of the Garzê–Litang ocean in the late Permian. Conversely, Paleozoic rocks are rarely exposed in the EYA. The EYA is dominated by Triassic volcanic-sedimentary sequences, which, from base to upward, include the Qugasi (sandstone, slate, phyllite, interbedded limestone, and basalt), Tumugou (conglomerate sandstone, slate, limestone, rhyolite, and andesite), Lanashan (sandstone, slate, and interbedded limestone), and Lamaya (slate and sandstone) formations (Wang et al., 2013a). Other strata younger than Triassic are absent in the whole Yidun arc.

Magmatic rocks in the Yidun arc (Fig. 1) were mainly formed in the Late Triassic (ca. 230–206 Ma) and Late Cretaceous (ca. 88–80 Ma) (Tian et al., 2019). The late Triassic magmatic rocks are both intrusive and extrusive and were formed by westward subduction of the Garzê–Litang Paleo-Tethyan Ocean (Wu et al., 2017). These rocks are mainly in intermediate to felsic composition. The Cretaceous igneous rocks are plutonic and include (biotite) granite, monzogranite, and granitic porphyry, which were formed in an intraplate extensional setting (Wang et al., 2019).

The DCGB in the EYA intrude into the Triassic volcanic sedimentary successions and is composed of granite, granodiorite, and minor quartz diorite(Fig. 2a). MMEs, which have ellipsoidal and lenticular shapes (typically 20–60 cm in diameter) and igneous texture, are randomly distributed in the DCGB (Fig. 2b-e). The host granitoids have equigranular texture, massive structure, and are mainly composed of plagioclase (30 to 45 vol%), K-feldspar (5 to 20 vol%), quartz (20 to 30 vol%), biotite (5 to 10 vol%), and hornblende (3 to 5% vol%) (Fig. 2f-g).

Accessory minerals include zircon, apatite, and titanite. Based on the relative proportion of melanocratic minerals inside, the MMEs can be divided into two types: Type-I MMEs consist mainly of plagioclase (40 to 45 vol%), amphibole (20 to 35% vol%), biotite (15 to 20% vol%), and quartz (<5% vol%) (Fig. 2b, j-l); Type-II MMEs are composed of amphibole (10 to 25%), biotite (10 to 15% vol%), plagioclase (45 to 55% vol%), and quartz (5 to 10% vol%) (Fig. 2c, h, i). Both types of MMEs show fine-grained hypidiomorphic texture and develop abundant acicular apatite (Fig. 2h,k). Field observation shows that Type-I and Type-II MMEs are transitionally in contact with the host granitoids (Fig. 2d). Petrography analyses reveal that plagioclase and quartz phenocrysts in the MMEs show similar size and morphology to those in the host granitoid (Fig. 2c-e), suggesting the transport of these minerals from granitoids to MMEs.

3. Analytical methods

3.1. Bulk chemical composition analyses

Fouty-one samples (18 granitoid, 5 Type-I MMEs, and 18 Type-II MMEs) were collected from the DCGB. Whole-rock major element analyses of these samples were conducted at ALS Chemex Co., Ltd., China, using X-ray fluorescence spectrometry (XRF), with an analytical uncertainty of better than 3% for the elements >1 wt% and 10% for elements <1 wt%. Trace elements analyses of these samples were based on Agilent 7900 inductively coupled plasma mass spectrometry (ICP-MS) at the Institute of Geochemistry, Chinese Academy of Sciences (IGCAS), with analytical uncertainty of better than 5% for the trace elements reported.

3.2. Mineral composition microanalyses

The mineral composition of plagioclase, amphibole, and biotite from granitoid and MMEs were analyzed using an EMP-1600 electron probe at the IGCAS, with detection limits of 0.01 wt% and analytical reproducibility of <2%.

3.3. LA-ICP-MS zircon U-Pb dating

Zircon grains were extracted from both granitoid and MMEs using heavy liquid and magnetic techniques. About 60 zircon grains for each sample were mounted in epoxy resin, which was polished to expose the grain interiors for analyses. Cathodoluminescence (CL) images of zircon were obtained using a JSM-7088F type thermal field scanning electron microscope equipped with a Gatan Mono CL4 detector at the IGCAS. All zircons were observed under transmitted/reflected-light and CL images to examine their inner structure, crack, and mineral inclusion for the selection of suitable crystal and test points, prior to U-Pb isotopic analyses.

Zircon in situ U-Pb isotopic analyses was performed using a GeoLas Pro 193 nm ArF excimer laser couped on an Agilent 7900 ICP-MS at the IGCAS (Liu et al., 2008). Zircon 91500 was used as a reference standard to normalize isotopic fractionation and was analyzed twice every 10 analyses. NIST 610 glass was used as an external standard to normalize U, Th, Pb contents of unknowns. Reference zircon Plesovice was used for data quality monitoring. Off-line selection and integration of background and analytic signals, and time-drift correction and quantitative calibration for U-Pb dating were performed by the ICPMSDataCal program. The age calculations and the plotting of concordia diagrams were made using Isoplot/Ex_ver4.15 (Ludwig, 2003).

3.4. Hg concentration and isotopic composition analyses

Total Hg concentration (THg) was measured by Lumex RA-915 + Hg analyzer equipped with a PYRO-915+ attachment (Russia) at the IGCAS, with a detection limit of 0.5 ng/g. Standard reference material GSS-4 (soil) was simultaneously tested and yielded THg recoveries of 90 to 110%. Analyses of sample duplicates show uncertainty <10%. Based on the measured THg concentrations, sample powders containing 25 ng Hg were weighted for Hg pre-concentration, using a double-stage tube furnace (Zerkle et al., 2020). The preconcentrated solution was diluted to 0.5 ng/mL Hg isotope and measured by a Neptune Plus MC-ICP-MS at the IGCAS, following an established method (Yin et al., 2016). Hg isotope compositions were reported following convention (Blum and Bergquist, 2007). MDF is expressed in δ^{202}Hg notation in units of ‰ referenced to NIST-3133 Hg standard (analyzed before and after each

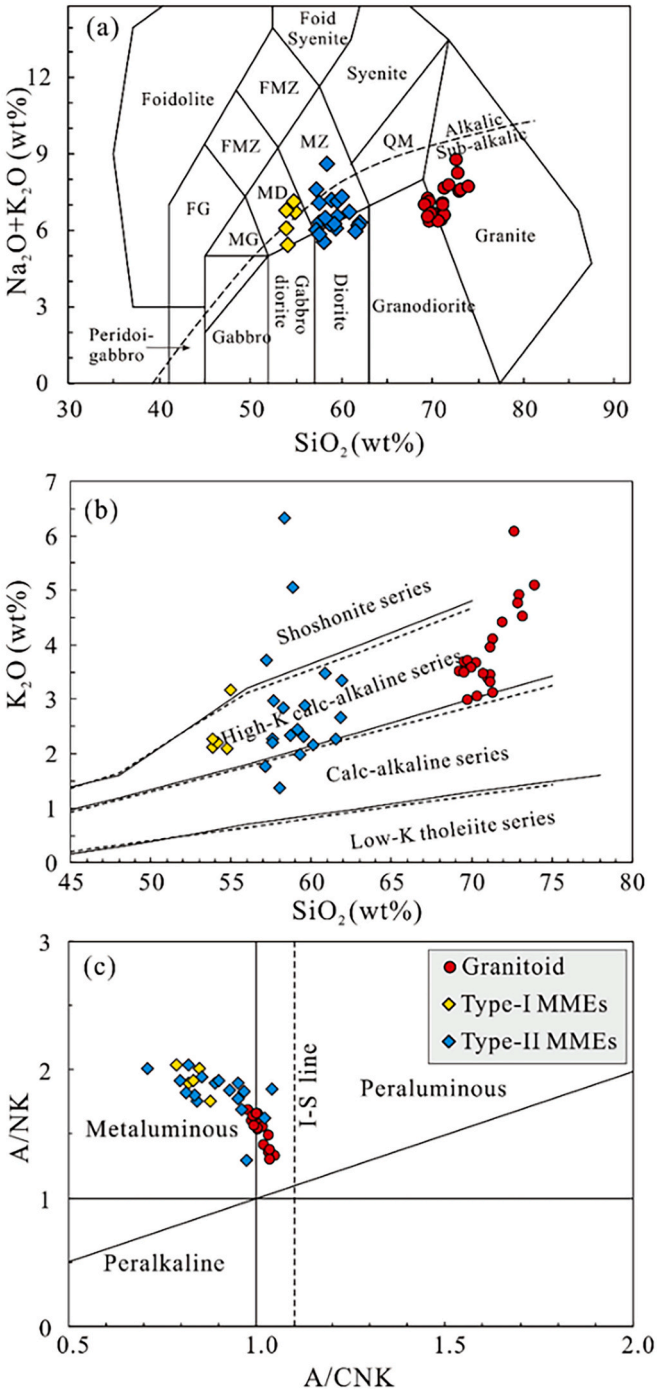

Fig. 3. Geochemical classification of granitoid and MMEs from the DCGB. (a) Total alkalis vs. silica diagram (after Middlemost, 1994); (b) K_2O vs. SiO_2 diagram (after Rickwood, 1989); (c) A/NK vs. A/CNK diagram (after Maniar and Piccoli, 1989).

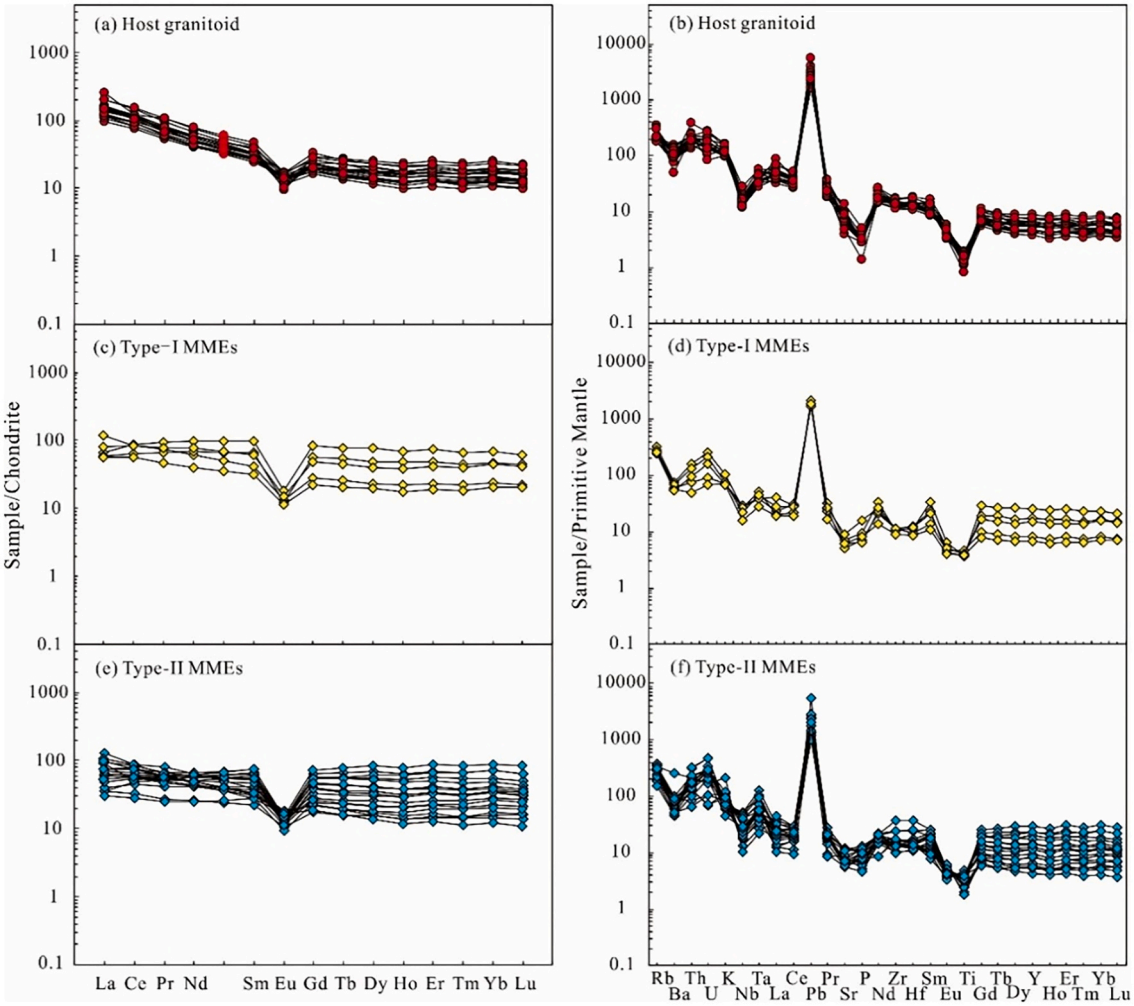

Fig. 4. Chondrite-normalized REE and primitive mantle-normalized multi-element patterns for granitoid and MMEs from the DCGB.

sample):

$$\delta^{202}Hg(‰) = \left[\left({}^{202}Hg/{}^{199}Hg_{sample}\right)/\left({}^{202}Hg/{}^{199}Hg_{NIST-3133}\right) - 1\right] \times 1000$$

MIF is reported in Δ notation, which represents the differences between the measured $\delta^{xxx}Hg$ and the theoretically predicted $\delta^{xxx}Hg$, in units of ‰:

$$\Delta^{xxx}Hg = \delta^{xxx}Hg - \delta^{xxx}Hg \times \beta$$

β is 0.252 for ^{199}Hg, 0.5024 for ^{200}Hg, and 0.7520 for ^{201}Hg. NIST 3177 secondary standard solution was measured in every 10 samples to monitor the data quality. The overall average and uncertainty of NIST-3177 ($\delta^{202}Hg = -0.59 \pm 0.10‰$; $\Delta^{199}Hg = 0.01 \pm 0.03‰$; $\Delta^{200}Hg = 0.02 \pm 0.03‰$; $\Delta^{201}Hg = -0.01 \pm 0.08‰$; 2SD, $n = 4$) are in good agreement with the reported values (Bergquist and Blum, 2007).

4. Results

4.1. Whole-rock major and trace elements

Major/trace elements concentrations are given in Table S1. Granitoids have the highest SiO_2 (69.3 to 73.3 wt%), but the lowest CaO (1.38 to 3.41 wt%), Fe_2O_3 (1.97 to 3.79 wt%) and MgO (0.27 to 1.24 wt%) contents. Type-I MMEs have the lowest SiO_2 (53.8 to 55.0 wt%), but the highest CaO (5.16 to 6.76 wt%), Fe_2O_3 (9.94 to 12.2 wt%) and MgO (3.26 to 3.61 wt%) contents, with $Mg^{\#}$ (molar Mg/(Mg + Fe)) = 35 to 42. Type-II MMEs have moderate SiO_2 (57.2 to 61.9 wt%), CaO (3.38 to 6.44 wt%), Fe_2O_3 (5.94 to 10.2 wt%), and MgO (1.60 to 5.13 wt%) contents, with $Mg^{\#} = 26$ to 59. All samples have low Loss On Ignition (LOI, typically <1.2%). In the total alkalis-silica diagram (Fig. 3a), granitoids fall into the granodiorite and granite fields, Type-I MMEs are in the monzodiorite field, Type-II MMEs are in the diorite and monzonite fields.

All the granitoids and MMEs have low TiO_2 (0.18 to 1.06 wt%), P_2O_5 (0.03 to 0.34 wt%), and MnO (0.05 to 0.30 wt%) contents, but high $Na_2O + K_2O$ (5.45 to 8.63 wt%) contents, belonging to high-K calc-alkaline rock (Fig. 3b). They also have relatively lower A/CNK (molar $Al_2O_3/CaO + Na_2O + K_2O$) values (0.71 to 1.05), showing metaluminous to weakly peraluminous affinity (Fig. 3c). In the Harker diagrams, they display coherent and linear geochemical trends for most selected elements (Fig. S1).

In the chondrite-normalized rare earth element (REE) diagram (Fig. 4), granitoids display right-inclined REE patterns, showing the enrichment in light REE (LREE) relative to heavy REE (HREE) with $(La/Yb)_N$ ratios of 4.86 to 15.4 and negative Eu anomalies (Eu/Eu*: 0.27 to 0.69). Type-I and Type-II MMEs show similar REE patterns that are characterized by LREE enrichment and nearly flat HREE with $(La/Yb)_N$ ratios of 0.67 to 8.89 and negative Eu anomalies (Eu/Eu*: 0.20 to 0.71). In the primitive mantle-normalized multi-element diagram (Fig. 4), all the granitoids and MMEs display arc-like elemental patterns that are enriched in large ion lithophile elements (LILE, e.g., Rb, Th, U, K, Pb) but depleted in high field strength elements (HFSE, e.g., Nb, Ta, Ti, P).

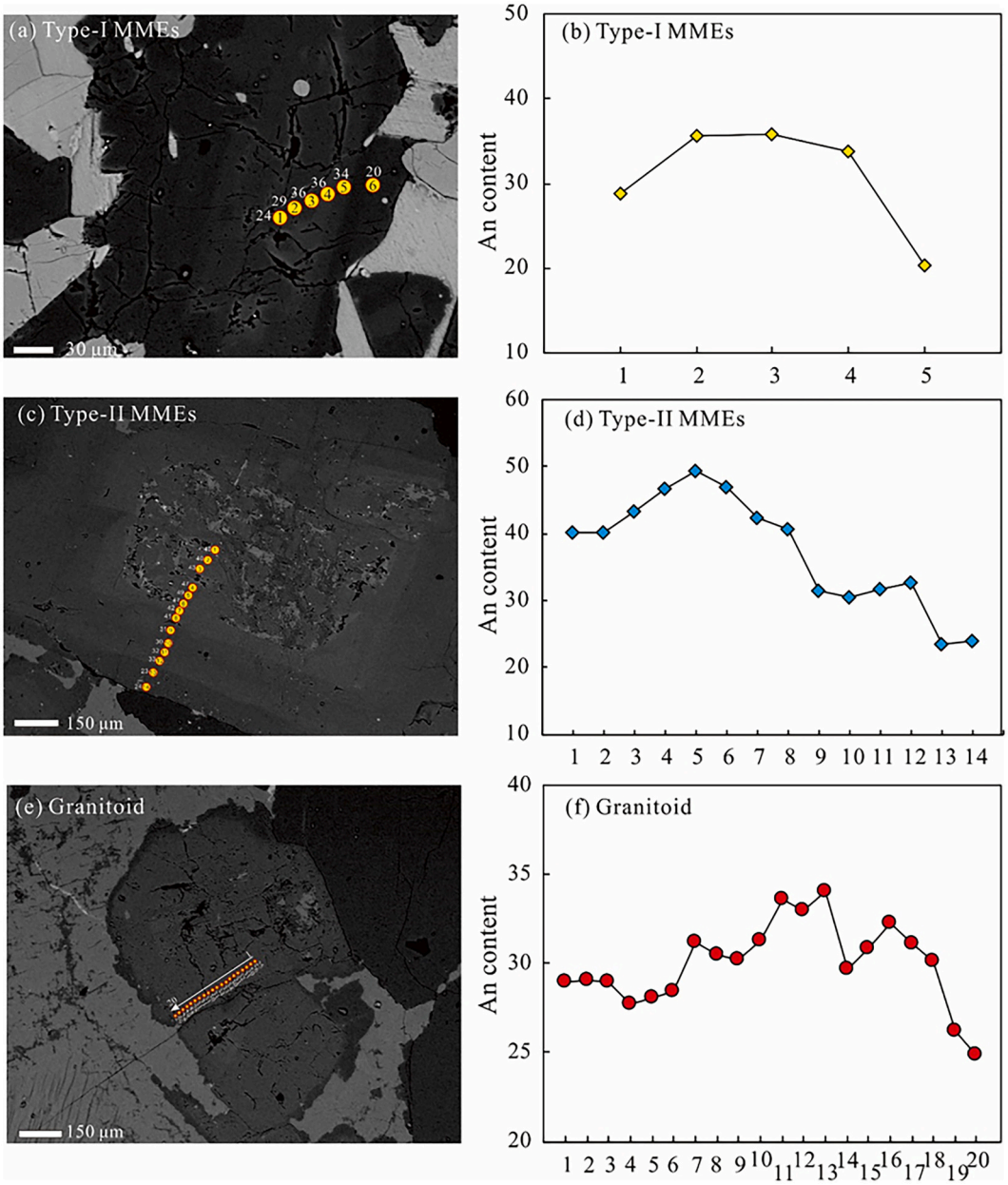

Fig. 5. BSE images and An value profiles of plagioclase from (a) Type-I MMEs, (b) Type-II MMEs, and (c) host granitoid.

4.2. Mineral chemical composition

Amphibole in granitoids, Type-I, and Type-II MMEs show similar chemical composition (Table S2), characterized by high FeO^T (21.9 to 24.8 wt%) but low MgO (6.71 to 9.43 wt%) and Al_2O_3 (3.01 to 6.83 wt %) contents, with $Mg^{\#}$ of 0.37 to 0.49. Almost all amphiboles belong to ferrohornblende (Fig. S2). Plagioclases from both MMEs and granitoid display complicated compositional zoning and interior structure. The An values of plagioclase crystals from Type-I MMEs increase from core to mantle, and decrease from mantle to rim (Fig. 5a). Plagioclases from Type-II MMEs (Fig. 5b) have a resorbed core (An = 40 to 43) with an irregular boundary. The core is abruptly surrounded by Ca-rich idiomorphic zone (An = 41 to 49), which is successively bordered by another zone (An = 31 to 33). The outmost rim of the plagioclase crystal is Na-rich (An = 23 to 24). Plagioclases from the host granitoid show fluctuated An values (25 to 34). All the analyzed plagioclases are oligoclase and andesine (Fig. S2).

Biotite in granitoids, Type-I, and Type-II MMEs show similar chemical compositions, characterized by high FeO^T (25.48 to 28.30 wt %) and TiO_2 (2.22 to 4.39 wt%) contents but relatively low MgO (5.72 to 7.48 wt%) contents. All of them fall into the primary biotite field (Fig. S2) and belong to Fe-biotite (Fig. S2).

4.3. Zircon U-Pb geochronology

Zircon U-Pb dating results are given in Table S3. Zircons from two granitoid samples (DC16-38A and GZ16–20) are euhedral to subhedral and mainly 90 to 130 μm in length with length/width ratios of ~1.5:1 to 2:1. Most of them show clear oscillatory zoning and have high Th/U ratios (0.20 to 0.77), indicative of magmatic origin. Twenty-two zircon grains were analyzed for DC16-38A. Excluding 4 grains having older $^{206}Pb/^{238}U$ age (233 Ma, 252 Ma, 737 Ma, and 626 Ma), the remaining grains yielded a weighted mean $^{206}Pb/^{238}U$ age of 216 ± 1.4 Ma (MSWD = 0.1) (Fig. 6a). Twenty-five zircons were analyzed for sample GZ16–20. Three zircons have Neoproterozoic apparent age of 776 to 827 Ma, whereas the others yield a weighted mean $^{206}Pb/^{238}U$ age of

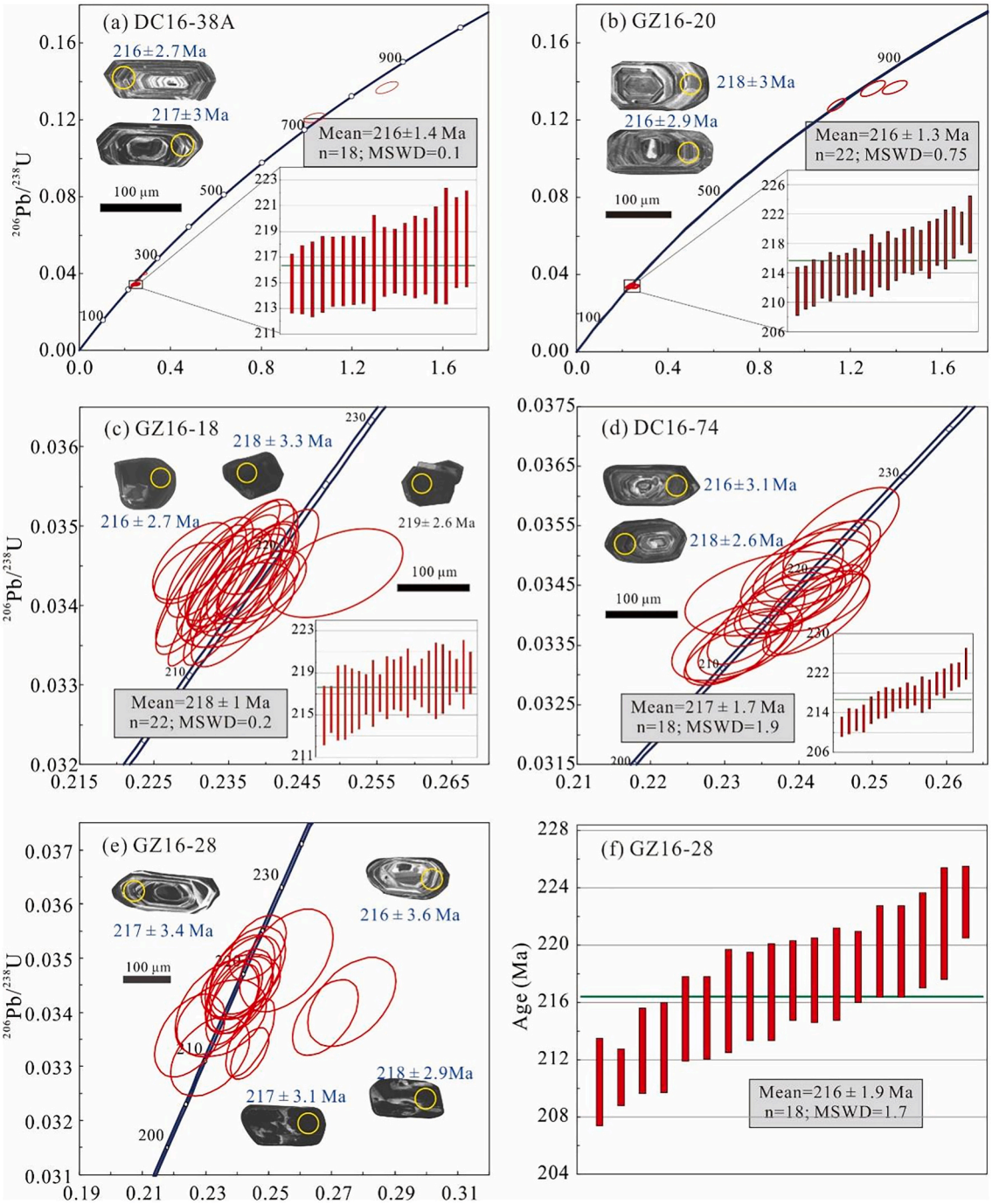

Fig. 6. Concordant diagrams of LA-ICP-MS zircon U-Pb dating results for host granitoid and MMEs from the DCGB.

216 ± 1.3 Ma (MSWD = 0.75) (Fig. 6b).

Zircons from a Type-I MME sample (GZ16–18) exhibit stubby and prismatic shapes, with sizes ranging from 70 to 100 μm and length/width ratios of ~1.1:1 to 1.3:1 (Fig. 6c). Most zircons show chaotic texture. They have Th/U ratios of 0.25 to 2.20, also indicative of magmatic origin. Analyses of 22 zircons from this sample yield a weighted mean $^{206}Pb/^{238}U$ age of 218 ± 1 Ma (MSWD = 0.20) (Fig. 6c).

Zircon grains from two type-II MMEs samples (GZ16–28 and DC16–74) are 80 to 130 μm long, with length/width ratios of ~1.2:1 to 3:1. These zircons have either oscillatory zoning or chaotic texture (Fig. 6e). They have high Th/U ratios of 0.41–1.23, suggesting their magmatic origin. Eighteen zircons from DC16–74 yield a weighted mean $^{206}Pb/^{238}U$ age of 217 ± 1.7 Ma (MSWD = 1.9) (Fig. 6d), and 18 zircons from GZ16–28 yield a weighted mean $^{206}Pb/^{238}U$ of 216 ± 1.9 Ma (MSWD = 1.7) (Fig. 6e).

4.4. THg concentration and isotope composition

Hg concentration and isotopic composition are given in Table S4 and Fig. S3. Granitoids have the lowest THg concentrations of 1.44 ± 1.00 ppb (SD, n = 18), Type-I and Type-II MMEs show relatively higher THg concentrations of 4.38 ± 2.39 ppb (SD, n = 3) and 2.48 ± 2.66 ppb (SD, n = 17), respectively.

Granitoids have different Hg isotope compositions from MMEs (Fig. 7a). The granitoids show the highest $\delta^{202}Hg$ values (−1.17 to 0.58‰) and negative to slightly positive $\Delta^{199}Hg$ values (−0.20 to

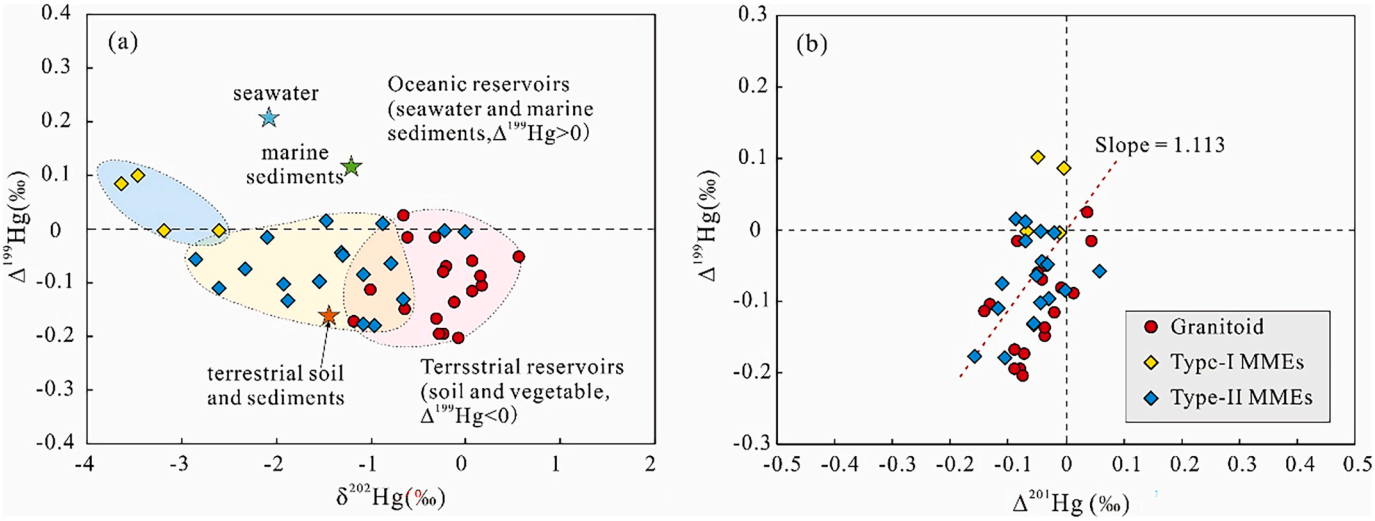

Fig. 7. Δ^{199}Hg vs. δ^{202}Hg (a) and Δ^{199}Hg vs. Δ^{201}Hg (b) for the samples from the DCGB.

0.02‰). Type-I MMEs have the lowest δ^{202}Hg values (−3.46 to −2.60‰) and slightly positive Δ^{199}Hg values (0.00 to 0.10‰). Type-II MMEs show intermediate δ^{202}Hg (−2.86 to −0.01‰) and Δ^{199}Hg values (−0.18 to 0.02‰).

5. Discussion

5.1. No evident Hg isotope fractionation during magmatic evolution of the DCGB

Granitoids and MMEs studied here show no obvious mineral alteration (Fig. 2), low LOI (mostly <1.2) and Chemical Index of Alteration (CIA <51) values, demonstrating limited influence by chemical weathering. The lack of negative correlation between $\varepsilon_{Nd}(t)$ and SiO_2 (Fig. S4) suggests that crustal contamination was also limited. The δ^{202}Hg values of granitoid and Type-I MMEs display no clear correlation with magmatic differentiation parameters (e.g., SiO_2) (Fig. S3), indicating fractional crystallization of silicate minerals is not likely the cause of Hg isotopic variation in these samples. Fluid exsolution and magma degassing may cause Hg-MDF. However, all our samples show Zr/Hf ratios (31.7 to 43.0) similar to that of chondrites (26 to 46, Bea et al., 2006), indicating the lack of fluid exsolution in these samples. Magma degassing results in the enrichment of lighter Hg isotopes in the gaseous Hg(0) phase, leaving the residue magma with higher δ^{202}Hg values (Zambardi et al., 2009), which cannot explain the overall negative δ^{202}Hg values in Type-I MMEs (−3.46 to −2.60‰) and granitoid (−1.17 to 0.58‰), despite a few positive δ^{202}Hg values. The δ^{202}Hg differences between granitoid and MMEs may be explained by different magma sources with distinct δ^{202}Hg signals, however, due to a lack of complete understanding of Hg-MDF during all magmatic processes, we feel it is unsafe to use δ^{202}Hg to trace magma sources. Below, however, we use Δ^{199}Hg to constrain the magma sources of our samples, given magmatic processes do not trigger Hg-MIF (Moynier et al., 2021; Wang et al., 2021a, 2021b; Yin et al., 2022).

5.2. Petrogenesis of the MMEs

Four models have been proposed for the origin of MMEs in intermediate to felsic intrusions: (1) entrainment of wall-rock xenolith (Vernon, 1984); (2) refractory and residual phase of partially melted source rock (Chappell et al., 1987); (3) mafic cumulate formed at the earlier stage of the same magmatic system (Dahlquist, 2002); and (4) hybridization between mafic and felsic magma (Barbarin, 2005). MMEs of restite or xenolith origins generally preserve the metamorphic or sedimentary fabric of the wall rocks (Qin et al., 2009). The studied MMEs have a typical igneous texture and identical zircon U-Pb age to the host granitoids, ruling out their refractory restite or wall-rock xenolith origins. The DCGB MMEs and host granitoids have previously shown overlapped bulk rock Sr-Nd (Fig. S4) and zircon Hf isotopes, which may imply a cumulate origin of the MMEs. However, the lack of cumulate texture, and the presence of disequilibrium textures, such as plagioclase with complex oscillatory zoning (Fig. 5), acicular apatite (Fig. 2k), and quartz ocelli (Fig. 2e), in our MMEs, suggest that the MMEs were formed via a rapid cooling process, possibly through injection of high-temperature mafic magma into low-temperature felsic melts (Vernon, 1984). The distinct Δ^{199}Hg values between the studied MMEs and granitoids (Fig. 7), instead, suggest that they were formed by magma mixing. Such mixing is supported by correlations between major/trace element concentrations or ratios (e.g., Na_2O/CaO vs. FeO/Al_2O_3, CaO/MgO vs. MgO, Al_2O_3/MgO vs. MgO, and Cs/Sr vs. Cs, Al_2O_3/CaO vs. Na_2O/CaO and K_2O/CaO vs. Al_2O_3/CaO) in our samples (Fig. S5). The previously reported similar Sr-Nd-Hf isotopes between the DCGB MMEs and granitoids (Dong et al., 2021) were likely resulted from isotopic equilibration (Lesher, 1990) and complex crystallization process (Wu et al., 2020) during magma mixing.

In this study, although a few MMEs have low $Mg^{\#}$, Cr, and Ni contents comparable to the rock generated by partial melting of the mafic lower crust, most of the MMEs display high $Mg^{\#}$ (up to 59), Cr (up to 177 ppm), and Ni (up to 85.3 ppm) contents, implying significant contribution from mantle materials. Notably, all the MMEs have high Co and V contents than the rock generated by partial melting of the mafic lower crust (Zhao et al., 2007). On the Harker diagram (Fig. S1), Fe_2O_3, MgO, CaO, TiO_2, and P_2O_5 show negative correlations with SiO_2, indicating strong fractional crystallization of olivine, clinopyroxene, Fe-Ti oxides, and apatite. Because olivine and clinopyroxene contain high MgO and Cr contents, fractional crystallization of them will result in low MgO and Cr content in the residual magma. We, therefore, suggest that the low-$Mg^{\#}$ MMEs may have undergone stronger crystallization differentiation of olivine and clinopyroxene than the high-$Mg^{\#}$ ones. Thus, we interpret that these MMEs most likely represent mantle-derived mafic magma that experienced significant crystal fractionation.

The strongly positive Δ^{199}Hg values in Type-I MMEs possibly suggest the contribution of Hg from recycled marine sediments, given marine sediments have large positive Δ^{199}Hg values (Yin et al., 2015; Yin et al., 2017). Large differences in Δ^{199}Hg have been observed in the primitive mantle (0.00 ± 0.10‰), terrestrial (soil and vegetation, −0.6 to 0‰) and oceanic (marine sediments and seawater, 0 to 0.4‰) reservoirs (Moynier et al., 2021; Blum et al., 2014). Type-I MMEs display nearly-

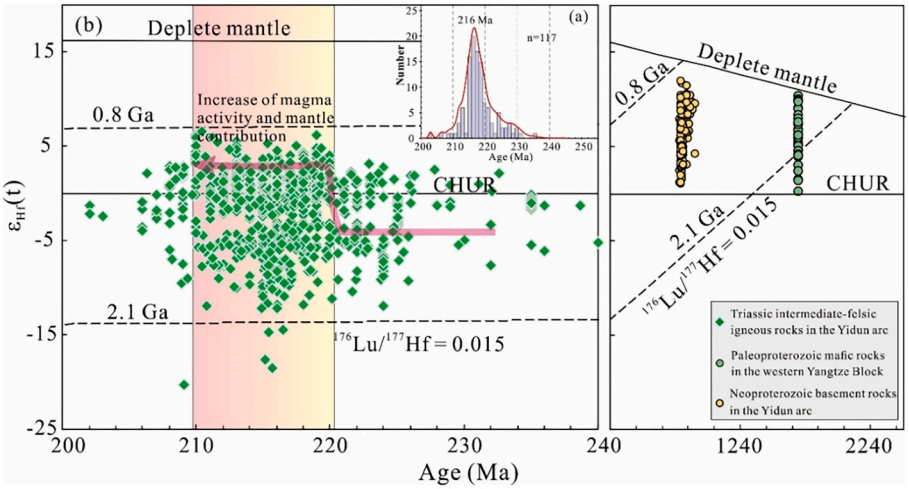

Fig. 8. $\varepsilon_{Hf}(t)$ vs. crystallization age for the granitoid and MMEs from the DCGB. The data of Triassic igneous rocks are from Cao et al. (2016), Dong et al. (2021), Gao et al. (2018), Leng et al. (2012, 2014, 2018), Peng et al. (2014), Reid et al. (2007), Wang et al. (2019), and Wu et al. (2017); Paleoproterozoic mafic rocks in the western Yangtze Block are from Wang et al. (2013c, 2013d) and Zhao et al. (2010); Neoproterozoic basement rock in the Yidun arc are from Tian et al. (2020).

zero to positive Δ^{199}Hg signals (Fig. 7), with $\Delta^{199}Hg/\Delta^{201}$Hg of 1.1, consistent with that observed during aqueous Hg(II) photoreduction in the Earth's surface environment (Bergquist and Blum, 2007). This suggests that the observed Δ^{199}Hg signals in the Type-I MMEs were originally inherited from Earth's surface reservoirs (e.g., marine sediments), which were recycled into the mantle source through subduction of the Garzê-Litang Paleo-Tethyan Ocean. During subduction, Hg tends to release from the subducted marine sediments, resulting in positive Δ^{199}Hg values in the subduction-related fluid/melt metasomatized lithospheric mantle. Buck rock chemical compositions, e.g., enrichment in LILE (e.g., Rb, Ba, Th, U), with pronounced negative Nb, Ta, Ti but positive Pb anomalies (Fig. 4), also support that the Type-I MMEs were originated from subduction-related fluid/melt modified mantle source.

The Type-II MMEs, which transitional contact with Type-I MMEs and granitoid (Fig. 2d), have intermediate major/trace elements and Hg isotope compositions (Fig. S3, and 7a), strongly suggesting that they were generated by mixing of varied proportions of magmas for (1) Type-I MMEs and (2) granitoids. The source magma for granitoids is likely crustal-derived felsic melts that have negative Δ^{199}Hg values, as discussed below.

5.3. Petrogenesis of the granitoid

Granitoids studied here show low Zr (127 to 199 ppm), Zr + Nb + Ce + Y (188 to 307 ppm) contents, and 10,000 × Ga/Al (1.9 to 2.5) ratios, precluding their A-type origin. I-type granitoid is characterized by the presence of amphibole with low A/CNK values (typically <1.1), whereas S-type granitoid generally contains peraluminous minerals (e.g., cordierite, garnet, or muscovite), with high A/CNK ratios (>1.1) (Maniar and Piccoli, 1989). The studied granitoids develop amphibole and have lower A/CNK values (0.98 to 1.05), indicating their I-type origin.

Several models have been proposed for the petrogenesis of the DCGB granitoids: (1) remelting of mafic to intermediate meta-igneous rocks in the middle-lower crust (Peng et al., 2014); (2) fractional crystallization of mantle-derived magma (Zhan et al., 2021); (3) melting of a mixed source of the Kanding Complex and basement sediments (Wu et al., 2017); and (4) mixing of crustal-derived and mantle-derived magma (He et al., 2013). Some scientists argued that granitoids in the DCGB were possibly generated via partial melting of Meso- to Paleoproterozoic mafic basement rocks (e.g, ~1.7 Ga amphibolite), which have identical composition to the coeval meta-igneous rock in the western Yangtze Block (Dong et al., 2021). However, given their positive $\varepsilon_{Hf}(t)$ (0.3 to 10.4; Zhao et al., 2010; Wang et al., 2013c) and $\varepsilon_{Nd}(t)$ (−0.2 to 3.8; Wang et al., 2013d) values, the Meso- to Paleoproterozoic mafic to intermediate rocks in the western Yangtze Block were originated from a depleted mantle source (Zhao et al., 2010; Wang et al., 2013d), which should have near-zero Δ^{199}Hg values (Moynier et al., 2021). Granitoids in the DCGB mostly show negative Δ^{199}Hg values (−0.20 to 0.02‰), precluding the possibility of partial melting of Meso- to Paleoproterozoic mafic basement rocks. Fractional crystallization of contemporaneous mantle-derived mafic magma can also be ruled out (Zhan et al., 2021), given that coeval mafic-ultramafic rocks are rare in the Yidun arc. Zircon Hf isotope evidence indicates that the DCGB granitoids have Paleo- and Meso-proterozoic model age (T_{DM2} = 1369–2035 Ma), which is older than the Kangding complex (797–795 Ma, zircon SHRIMP U-Pb; Zhou et al., 2002). The large variation of $\varepsilon_{Hf}(t)$ (−12.2 to −3.7) (Dong et al., 2021), $\varepsilon_{Nd}(t)$ (−9.5 to −5.7) (Fig. S4), and negative to slightly positive Δ^{199}Hg values (−0.20 to 0.02‰) strongly suggest that these granitoids were formed by mixing of crustal-derived melt with mantle-derived magma.

A mixed genesis is further evidenced by the fact that some plagioclase crystals from the host granitoid exhibit fluctuated An contents (Fig. 5), which suggests multiple injections of mafic melt into the felsic magma chamber during the formation of granitoid. We refer that the reworking of intracrustal sediments by mantle-derived magma, with the subsequent mixing of the two melts, is likely the main mechanism to produce I-type granitoid in the DCGB. Low Sr/Y (typically 1.99 to 9.17), Zr/Hf (34 to 41), P_2O_5 (0.03 to 0.11 wt%) contents, and marked negative Eu (Eu/Eu*: 0.27 to 0.69) anomalies suggest that feldspar, zircon, and apatite have been fractionated during the evolution of the DCGB granitic magma.

6. Conclusions and implications for the petrogenetic model

Triassic magmatism in the Yidun arc lasted nearly ~30 Ma (235 to 208 Ma, Fig. 8). During the early stages (235 to 220 Ma), the magmatic activity was relatively weak and mainly induced reworking of ancient continental crust, as suggested by the negative-dominantly $\varepsilon_{Hf}(t)$ values. The magmatism was significantly increased from 220 Ma and reached a peak at ~216 Ma, accompanied by the crescent contribution of mantle materials. The generation of such large-scale intermediate-felsic magmatism during this period indicates that a critical geodynamic event occurred, which result in strong crust-mantle interaction and widespread crustal anatexis. The presence of abundant ~220–240 Ma proximal-deposited detrital zircon derived from coeval arc magmatic rocks in upper Triassic sandstone indicates rapid tectonic uplift of Yidun

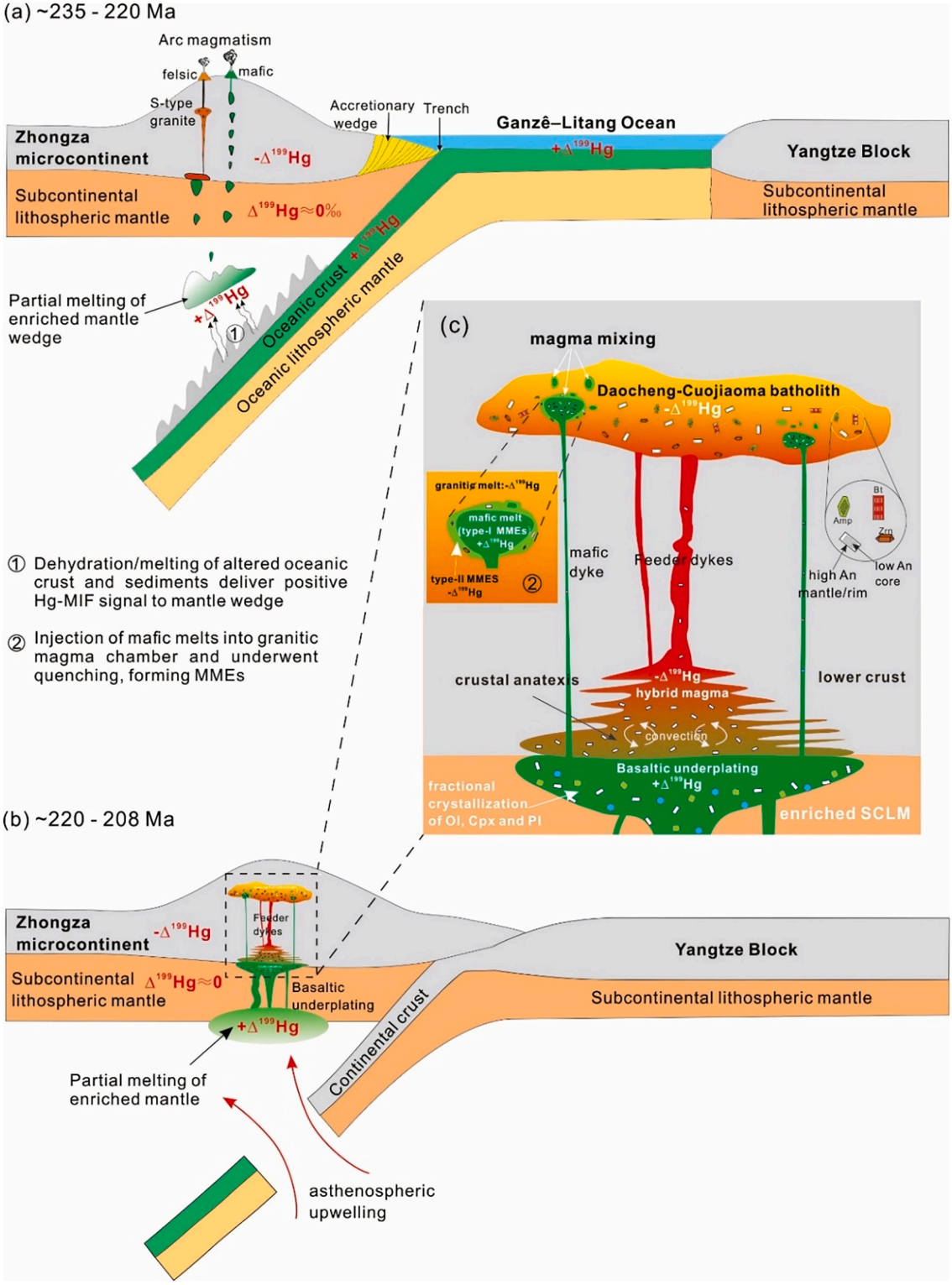

Fig. 9. Schematic illustration for the tectonic evolution and generation of granitoid and MMEs in the Yidun arc, eastern Tibetan Plateau. (a) Ca. 235–220 Ma, the Garzê–Litang Paleo-Tethys subducted beneath the Zhongza microcontinent, which resulted in the partial melting of lithospheric mantle and overlying lower crust, producing minor arc magmatic rocks, such as the ~230 Ma dacite (Wang et al., 2013b) and 224 Ma Ajisenduo S-type granite (Wu et al., 2017). (b) During 220–208 Ma, abundant magmatic activities were triggered by slab breakoff. Partial melting of subduction fluid/melt metasomatized mantle wedge generated large amounts of mafic magma that underplated in the lower crust, and resulted in crustal anatexis to generate granitic melt. Interaction of mantle-derived mafic melt ($+\Delta^{199}$Hg) and crustal-derived felsic melt ($-\Delta^{199}$Hg) produced the hybrid granitic melts with negative Δ^{199}Hg values, which were extracted to ascend and pond in the shallow crust to form the DCGB. Then, minor evolved basaltic magma was injected into the unconsolidated granitic magma chamber, generating the observed mafic enclaves in the batholith.

arc in the Late Triassic (Wang et al., 2013a). Rapid uplift, combined with the blueschist-facies metamorphism (Gu et al., 1996), is consistent with the scenario of slab breakoff (von Blanckenburg and Davies, 1995). Thus, we suggest that magma flare-up at 220–208 Ma (with a peak of 216 Ma) in the Yidun arc was probably related to slab breakoff.

We propose that, during the early stage (235 to 220 Ma) of oceanic crust subduction, partial melting of lithospheric mantle produced minor basaltic magma, as represented by Changtai basalt (Wang et al., 2013b), which resulted in crustal anatexis, generating felsic igneous rocks (e.g., ~224 Ma Ajisenduo S-type granite, and ~ 230 Ma Changtai rhyolite) (Fig. 9a). As subduction proceeded, the Garzê–Litang ocean slab was broken off at ca. 220 Ma, which led to upwelling of asthenosphere mantle and subsequently extensive melting of subduction fluid/melt metasomatized mantle wedge. The resultant mafic magma, which has positive Δ^{199}Hg values, may underplate at the bottom of the lower crust, and experience fractional crystallization of olivine, clinopyroxene, and plagioclase. The underplating of mafic magma provided sufficient heat to melt the lower crust, which produces large amounts of felsic melt with negative Δ^{199}Hg values. Extensive interaction of basaltic and felsic melts in the lower crust produced the hybrid melts (Fig. 9b), which were then extracted to ascent and ponded in the shallow crust, and experienced fractional crystallization of feldspar, zircon, and apatite. Prior to the consolidation of the shallow magma chamber, some evolved mafic magma, as represented by Type-I MMEs, may migrate upward and inject into the granitic magma chamber (Fig. 9c). Mixing of mafic and granitic magma generated the Type-II MMEs.

Declaration of Competing Interest

The authors declare that they have no known competing financial interestsor personal relationships that could have appeared to influence the work reported in this paper.

Acknowledgments

This study was supported by the National Natural Science Foundation of China (41873047, 42102277), China Postdoctoral Science Foundation (2021M703188), and the Second Tibetan Plateau Scientific Expedition and Research (2021QZKK0301).

Appendix A. Supplementary data

Supplementary data to this article can be found online at https://doi.org/10.1016/j.chemgeo.2022.120974.

References

Barbarin, B., 2005. Mafic magmatic enclaves and mafic rocks associated with some granitoids of the Central Sierra Nevada batholith, California: nature, origin, and relations with the hosts. Lithos 80 (1–4), 155–177.
Bea, F., Montero, P., Ortega, M., 2006. A LA–ICP–MS evaluation of Zr reservoirs in common crustal rocks: implications for Zr and Hf geochemistry, and zircon-forming processes. Can. Mineral. 44, 693–714.
Bergquist, B.A., Blum, J.D., 2007. Mass-dependent and -independent fractionation of hg isotopes by photoreduction in aquatic systems. Science 318 (5849), 417–420.
Blum, J.D., Bergquist, B.A., 2007. Reporting of variations in the natural isotopic composition of mercury. Anal. Bioanal. Chem. 388 (2), 353–359.
Blum, J.D., Sherman, L.S., Johnson, M.W., 2014. Mercury isotopes in earth and environmental sciences. Annu. Rev. Earth Planet. Sci. 42 (1), 249–269.
Cao, K., Xu, J.-F., Chen, J.-L., Huang, X.-X., Ren, J.-B., Zhao, X.-D., Liu, Z.-X., 2016. Double-layer structure of the crust beneath the Zhongdian arc, SW China: U–Pb geochronology and Hf isotope evidence. J. Asian Earth Sci. 115, 455–467.
Chappell, B.W., White, A.J.R., Wyborn, D., 1987. The importance of residual source material (restite) in granite petrogenesis. J. Petrol. 28 (6), 1111–1138.
Chen, J.L., Xu, J.F., Ren, J.B., Huang, X.X., Wang, B.D., 2014. Geochronology and geochemical characteristics of Late Triassic porphyritic rocks from the Zhongdian arc, eastern Tibet, and their tectonic and metallogenic implications. Gondwana Res. 26 (2), 492–504.
Dahlquist, J.A., 2002. Mafic microgranular enclaves: early segregation from metaluminous magma (Sierra de Chepes), Pampean Ranges, NW Argentina. J. S. Am. Earth Sci. 15 (6), 643–655.
Dong, P., Dong, G., Santosh, M., Mo, X., Wang, P., Li, H., Tang, J., Su, L., Sun, Z., Ketchaya, Y.B., 2021. Multiple sources and magmatic evolution of the Late Triassic Daocheng batholith in the Yidun Terrane: implications for evolution of the Paleo-Tethys Ocean in the eastern Tibetan Plateau. Geol. Soc. Am. Bull. 2021.
Gao, X., Yang, L.-Q., Orovan, E.A., 2018. The lithospheric architecture of two subterranes in the eastern Yidun Terrane, East Tethys: insights from Hf–Nd isotopic mapping. Gondwana Res. 62, 127–143.
Gu, D.L., Su, S.G., You, Z.D., 1996. The temporal-spatial distribution and origin of blueschist in China. Reg. Geol. China 04, 58–66.
He, D.F., Zhu, W.G., Zhong, H., Ren, T., Bai, Z.J., Fan, H.P., 2013. Zircon U–Pb geochronology and elemental and Sr–Nd–Hf isotopic geochemistry of the Daocheng granitic pluton from the Yidun Arc, SW China. J. Asian Earth Sci. 67-68, 1–17.
Kong, D.X., Xu, J.F., Chen, J.L., 2016. Oxygen isotope and trace element geochemistry of zircons from porphyry copper system: implications for Late Triassic metallogenesis within the Yidun Terrane, southeastern Tibetan Plateau. Chem. Geol. 441, 148–161.
Leng, C.-B., Zhang, X.-C., Hu, R.-Z., Wang, S.-X., Zhong, H., Wang, W.-Q., Bi, X.-W., 2012. Zircon U–Pb and molybdenite Re–Os geochronology and Sr–Nd–Pb–Hf isotopic constraints on the genesis of the Xuejiping porphyry copper deposit in Zhongdian, Northwest Yunnan, China. J. Asian Earth Sci. 60 (22), 31–48.
Leng, C.B., Huang, Q.Y., Zhang, X.C., Wang, S.X., Zhong, H., Hu, R.Z., Bi, X.W., Zhu, J.J., 2014. Petrogenesis of the Late Triassic volcanic rocks in the Southern Yidun arc, SW China: constraints from the geochronology, geochemistry, and Sr–Nd–Pb–Hf isotopes. Lithos 190-191, 363–382.
Leng, C.B., Gao, J.F., Chen, W.T., Zhang, X.C., Tian, Z.D., Guo, J.H., 2018. Platinum-group elements, zircon Hf-O isotopes, and mineralogical constraints on magmatic evolution of the Pulang porphyry Cu-Au system, SW China. Gondwana Res. 62, 163–177.
Lesher, C.E., 1990. Decoupling of chemical and isotopic exchange during magma mixing. Nature 344 (6263), 235–237.
Liu, Y.S., Hu, Z.C., Gao, S., Gunther, D., Xu, J., Gao, C.G., Chen, H.H., 2008. In situ analysis of major and trace elements of anhydrous minerals by LA-ICP-MS without applying an internal standard. Chem. Geol. 257 (1–2), 34–43.
Ludwig, K.R., 2003. ISOPLOT 3.00: A Geochronological Toolkit for Microsoft Excel. Berkeley Geochronology Center, Berkeley, California, pp. 1–71.
Maniar, P.D., Piccoli, P.M., 1989. Tectonic discrimination of granitoids. Geol. Soc. Am. Bull. 101 (5), 635–643.
Middlemost, E.A.K., 1994. Naming materials in the magma igneous rock system. Earth Sci. Rev. 37 (3–4), 215–224.
Moynier, F., Chen, J.B., Zhang, K., Cai, H.M., Wang, Z.C., Jackson, M.G., Day, J.M., 2020. Chondritic mercury isotopic composition of earth and evidence for evaporative equilibrium degassing during the formation of eucrites. Earth Planet. Sci. Lett. 551, 116544.
Moynier, F., Jackson, M.G., Zhang, K., Cai, H.M., Halldorsson, S.A., Pik, R., Day, J.M.D., Chen, J.B., 2021. The mercury isotopic composition of earth's mantle and the use of mass independently fractionated Hg to test for recycled crust. Geophys. Res. Lett. 48 (17) e2021GL094301.
Peng, T.P., Zhao, G.C., Fan, W.M., Peng, B.X., Mao, Y.S., 2014. Zircon geochronology and Hf isotopes of Mesozoic intrusive rocks from the Yidun terrane, Eastern Tibetan Plateau: petrogenesis and their bearings with Cu mineralization. J. Asian Earth Sci. 80 (2), 18–33.
Qin, J.F., Lai, S.C., Diwu, C.R., Ju, Y.J., Li, Y.F., 2009. Magma mixing origin for the post-collisional adakitic monzogranite of the Triassic Yangba pluton, Northwestern margin of the South China block: geochemistry, Sr–Nd isotopic, zircon U–Pb dating and Hf isotopic evidences. Contrib. Mineral. Petrol. 159 (3), 389–409.
Reid, A., Wilson, C.J.L., Shun, L., Pearson, N., Belousova, E., 2007. Mesozoic plutons of the Yidun Arc, SW China: U/Pb geochronology and Hf isotopic signature. Ore Geol. Rev. 31, 88–106.
Rickwood, P.C., 1989. Boundary lines within petrologic diagrams which use oxides of major and minor elements. Lithos 22 (4), 247–263.
Ruprecht, P., Bergantz, G.W., Cooper, K.M., Hildreth, W., 2012. The crustal magma storage system of Volcán Quizapu, Chile, and the effects of magma mixing on magma diversity. J. Petrol. 53 (4), 801–840.
Tian, Z.-D., Leng, C.-B., Zhang, X.-C., Zhou, L.-M., Tang, Y.-W., 2019. Recognition of Late Triassic Cu-Mo mineralization in the Northern Yidun Arc (S.E. Tibetan Plateau): implications for regional exploration. Minerals 9 (12), 765.
Tian, Z.D., Leng, C.B., Zhang, X.C., 2020. Provenance and tectonic setting of the Neoproterozoic meta-sedimentary rocks at southeastern Tibetan Plateau: implications for the tectonic affinity of Yidun terrane. Precambrian Res. 344, 105736.
Vernon, R.H., 1984. Microgranitoid enclaves in granites—globules of hybrid magma quenched in a plutonic environment. Nature 309 (5967), 438–439.
von Blanckenburg, F., Davies, J.H., 1995. Slab breakoff: a model for syncollisional magmatism and tectonics in the Alps. Tectonics 14 (1), 120–131.
Wang, B.Q., Zhou, M.F., Li, J.W., Yan, D.P., 2011. Late Triassic porphyritic intrusions and associated volcanic rocks from the Shangri-La region, Yidun terrane, Eastern Tibetan Plateau: adakitic magmatism and porphyry copper mineralization. Lithos 127, 24–38.
Wang, B.Q., Wang, W., Zhou, M.F., 2013a. Provenance and tectonic setting of the Triassic Yidun Group, the Yidun Terrane, Tibet. Geosci. Front. 4 (6), 765–777.
Wang, B.Q., Zhou, M.F., Chen, W.T., Gao, J.F., Yan, D.P., 2013b. Petrogenesis and tectonic implications of the Triassic volcanic rocks in the northern Yidun Terrane, Eastern Tibet. Lithos 175 (8), 285–301.
Wang, D.B., Yin, F.G., Sun, Z.M., Wang, L.Q., Wang, B.D., Liao, S.Y., Tang, Y., Ren, G.M., 2013c. Zircon U-Pb age and Hf isotope of Paleoproterozoic mafic intrusion on the western margin of the Yangtze Block and their implications. Geol. Bull. China 32 (04), 617–630 (in Chinese with English abstract).

Wang, S.W., Liao, Z.W., Sun, X.M., Jiang, X.F., Zhou, B.G., Guo, Y., Luo, M.J., Zhu, H.P., Ma, D., 2013d. Geochemistry of Paleoproterozoic diabases in the Dongchuan copper deposit, Yunnan, SW China: response to breakup of the columbia supercontinent in the southwestern margin of Yangtze Block. Acta Geol. Sin. 87 (12), 1834–1852 (in Chinese with English abstract).

Wang, X.-S., Bi, X.-W., Chen, Y.-W., Pan, L.-C., Xu, L.-L., 2019. Crystal fractionation of contaminated melts and re-melting of newly underplated basaltic crust generated Late Triassic andesitic and dioritic intrusions in the southern Yidun Terrane, SW China. Lithos 342-343, 135–151.

Wang, D.Z., Hu, R.Z., Hollings, P., Bi, X.W., Zhong, H., Pan, L.C., Leng, C.B., Huang, M.L., Zhu, J.J., 2021a. Remelting of a Neoproterozoic arc root: origin of the Pulang and Songnuo porphyry Cu deposits, Southwest China. Mineral. Deposita 56 (6), 1043–1070.

Wang, X., Deng, C., Yang, Z., Zhu, J.-J., Yin, R., 2021b. Oceanic mercury recycled into the mantle: evidence from positive Δ^{199}Hg in lamprophyres. Chem. Geol. 584, 120505.

Weislogel, A.L., 2008. Tectonostratigraphic and geochronologic constraints on evolution of the northeast Paleotethys from the Songpan-Ganzi complex, Central China. Tectonophysics 451 (1–4), 331–345.

Wu, T., Xiao, L., Wilde, S.A., Ma, C.-Q., Li, Z.-L., Sun, Y., Zhan, Q.-Y., 2016. Zircon U–Pb age and Sr–Nd–Hf isotope geochemistry of the Ganluogou dioritic complex in the northern Triassic Yidun arc belt, Eastern Tibetan Plateau: implications for the closure of the Garzê-Litang Ocean. Lithos 248-251, 94–108.

Wu, T., Xiao, L., Wilde, S.A., Ma, C.Q., Zhou, J.X., 2017. A mixed source for the Late Triassic Garzê-Daocheng granitic belt and its implications for the tectonic evolution of the Yidun arc belt, eastern Tibetan Plateau. Lithos 288-289, 214–230.

Wu, T., Zhang, W., Wilde, S.A., 2020. The origin of mafic microgranular enclaves in granitoids: insights from in situ Sr isotope of plagioclases and Zr-Hf isotopes of zircons. Chem. Geol. 551, 119776.

Yin, R., Feng, X., Chen, B., Zhang, J., Wang, W., Li, X., 2015. Identifying the sources and processes of mercury in subtropical estuarine and ocean sediments using Hg isotopic composition. Environ. Sci. Technol. 49 (3), 1347–1355.

Yin, R., Feng, X., Hurley, J.P., Krabbenhoft, D.P., Lepak, R.F., Hu, R., Zhang, Q., Li, Z., Bi, X., 2016. Mercury isotopes as proxies to identify sources and environmental impacts of mercury in sphalerites. Sci. Rep. 6 (1), 18686.

Yin, R., Xu, L., Lehmann, B., Lepak, R.F., Hurley, J.P., Mao, J., Feng, X., Hu, R., 2017. Anomalous mercury enrichment in early Cambrian black shales of South China: mercury isotopes indicate a seawater source. Chem. Geol. 467, 159–167.

Yin, R., Chen, D., Pan, X., Deng, C., Chen, L., Song, X., Yu, S., Zhu, C., Wei, X., Xu, Y., Feng, X., Blum, J.D., Lehmann, B., 2022. Mantle Hg isotopic heterogeneity and evidence of oceanic Hg recycling into the mantle. Nat. Commun. 13, 948.

Zambardi, T., Sonke, J., Toutain, J.-P., Sortnob, F., Shinoharac, H., 2009. Mercury emissions and stable isotopic compositions at Vulcano Island (Italy). Earth Planet. Sci. Lett. 277, 236–243.

Zerkle, A.L., Yin, R., Chen, C., Li, X., Izon, G.J., Grasby, S.E., 2020. Anomalous fractionation of mercury isotopes in the Late Archean atmosphere. Nat. Commun. 11 (1), 1709.

Zhan, Q.Y., Zhu, D.C., Wang, Q., Cawood, P.A., Xie, J.C., Liu, X., Li, S.M., Zhang, L.L., Zhao, Z.D., 2021. Imaging the Late Triassic lithospheric architecture of the Yidun Terrane, eastern Tibetan Plateau: observations and interpretations. Geol. Soc. Am. Bull. 133 (11−12), 2279–2290.

Zhao, Z.-F., Zheng, Y.-F., Wei, C.-S., Wu, Y.-B., 2007. Post-collisional granitoids from the Dabie orogen in China: zircon U–Pb age, element and O isotope evidence for recycling of subducted continental crust. Lithos 93 (3–4), 248–272.

Zhao, X.F., Zhou, M.F., Li, J.W., Sun, M., Gao, J.F., Sun, W.H., Yang, J.H., 2010. Late Paleoproterozoic to early Mesoproterozoic Dongchuan Group in Yunnan, SW China: implications for tectonic evolution of the Yangtze Block. Precambrian Res. 182 (1–2), 57–69.

Zhou, M.-F., Yan, D.-P., Kennedy, A.K., Li, Y., Ding, J., 2002. SHRIMP U–Pb zircon geochronological and geochemical evidence for Neoproterozoic arc-magmatism along the western margin of the Yangtze Block, South China. Earth Planet. Sci. Lett. 196 (1–2), 51–67.